Blurring the Boundaries Between Topological and Nontopological Phenomena in Dots

Denis R. Candido,[1] Michael E. Flatté,[2,3] and J. Carlos Egues[1,3]

[1]*Instituto de Física de São Carlos, Universidade de São Paulo, 13560-970, São Carlos, São Paulo, Brazil*
[2]*Department of Physics and Astronomy and Optical Science and Technology Center,*
University of Iowa, Iowa City, Iowa 52242, USA
[3]*International Institute of Physics, Federal University of Rio Grande do Norte, 59078-970, P.O. Box 1613, Natal, Brazil*

We investigate the electronic and transport properties of topological and nontopological $InAs_{0.85}Bi_{0.15}$ quantum dots (QDs) described by a ~ 30 meV gapped Bernevig-Hughes-Zhang (BHZ) model with cylindrical confinement, i.e., "BHZ dots." Via modified Bessel functions, we analytically show that *nontopological* dots quite unexpectedly have discrete helical edge states, i.e., Kramers pairs with spin-angular-momentum locking similar to topological dots. These unusual nontopological edge states are geometrically protected due to confinement for a wide range of parameters and remarkably contrast with the bulk-edge correspondence in topological insulators, as no bulk topological invariant guarantees their existence. Moreover, for a conduction window with four edge states, we find that the two-terminal conductance $\mathcal{G}$ versus the QD radius R and the gate V_g controlling its levels shows a double peak at $2e^2/h$ for both topological and trivial BHZ QDs. This is in stark contrast to conductance measurements in 2D quantum spin Hall and trivial insulators. All of these results were also found in HgTe QDs. Bi-based BHZ dots should also prove important as hosts to room temperature edge spin qubits.

Introduction.—Topological insulators (TIs) are a new class of materials having the unusual property of being an insulator in bulk with robust gapless helical states localized near their edges (2D TIs) and surfaces (3D TIs) [1–4]. Following these pioneering works, a few other TI proposals [5–11] have been put forward with some experimental support [12,13]. More recently, topological quantum dots (QDs) with cylindrical confinement have been investigated [14–27]. Their spectra feature discrete helical edge states protected against nonmagnetic scattering and show spin-angular-momentum locking. These states are potentially important for spintronics [15,16], quantum computation, and other quantum technologies [14,17,18].

Here we demonstrate that *nontopological* QDs defined in InAsBi wells obeying the effective Bernevig-Hughes-Zhang (BHZ) model with cylindrical confinement—BHZ dots—feature helical edge states *geometrically protected* due to confinement (Fig. 1). This surprising result contrasts with the usual bulk-edge correspondence in TIs, as the nontopological dots here—despite having a zero bulk topological invariant—exhibit edge states with spin-angular-momentum locking similar to topological dots [14–25]. Interestingly, our quantum transport calculation shows that circulating currents [28,29] (Fig. 2) and the two-terminal linear conductance $\mathcal{G}$ [30] (versus the dot radius R and the gate V_g controlling its levels, Fig. 3) of nontopological and topological QDs are essentially identical. More specifically, for BHZ dots with two Kramers pairs of edge states,
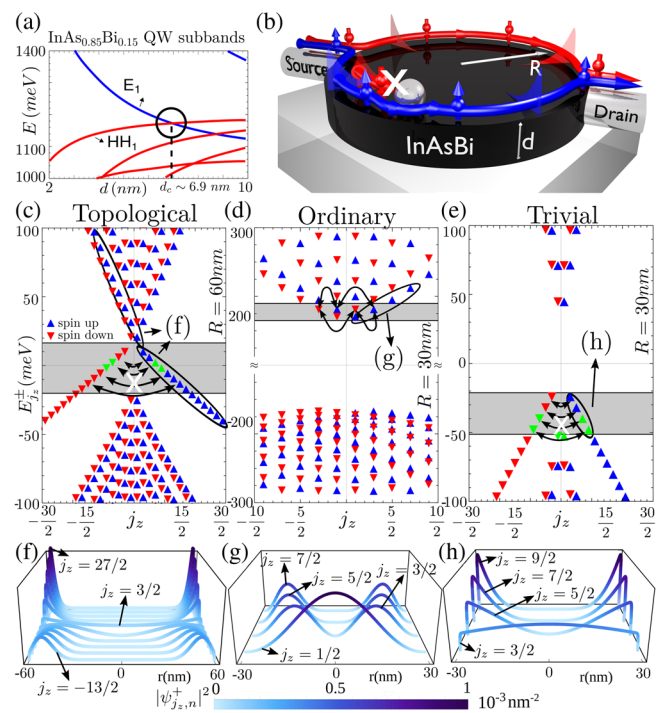
FIG. 1.   (a) $InAs_{0.85}Bi_{0.15}$ QW subbands versus the well thickness d. (b) Schematic of a cylindrical QD with helical edge states. Energy levels versus the total angular momentum j_z for (c) a topological $InAs_{0.85}Bi_{0.15}$ BHZ dot with $R = 60$ nm, (d) an ordinary (non-BHZ) InAs dot with $R = 30$ nm, and (e) a trivial $InAs_{0.85}Bi_{0.15}$ BHZ dot with $R = 30$ nm. The curved arrows denote the forbidden and allowed transitions. (f)–(h) Probability densities $|\psi_{j_z,n}^+|^2$ for the edge states in (c) and (d) and bulk states (g) (see ellipses).

$\mathcal{G}$ shows double-peak resonances at $2e^2/h$, separated by a dip due to destructive interference in both regimes. When bulk- and edge-state Kramers pairs coexist and are degenerate, both regimes show a single-peak resonance also at $\mathcal{G} = 2e^2/h$. Our findings blur the boundaries between topological and nontopological BHZ dots for the appearance of protected helical edge states and for the behavior of conductance measurements.

We also predict that InAs$_{1-x}$Bi$_x$/AlSb quantum wells (QWs) become 2D topological insulators for well widths $d > 6.9$ nm and $x = 0.15$, with large inverted subband gaps ~ 30 meV ($> k_B T$) that should enable room temperature applications [Fig. 1(a)]. Our BHZ dots are obtained by further confining these Bi-based wells with soft and hard walls. Our *analytical* QD eigenenergies and wave functions (Fig. 1) for both topological and nontopological regimes show that the helical edge states occur in a wide range of QD radii. We note that many Bi-containing compounds (including chalcogenides [4]) are known TIs, and InBi in monolayer or bilayer form [31] has been suggested to show nontrivial topological characteristics. Our findings also hold for HgTe-based systems (see Supplemental Material [32]).

New 2D topological insulator: InAs$_{0.85}$Bi$_{0.15}$/AlSb.— The response of the electronic structure of InAs to the addition of the isoelectronic dopant Bi [33–35] is well described within valence band anticrossing theory [53–56]. Bi provides a resonant state within the valence band (complementary to the resonant state in the conduction band generated in the dilute nitrides such as GaAs$_{1-x}$N$_x$), which strongly pushes up the valence band edge of InAs as Bi is added. The small band gap of InAs allows it to close for approximately 7.3% of Bi [33–35] and for inversion of the conduction and valence bands similar to HgTe for larger Bi percentage. We determine the electronic states of an InAs$_{1-x}$Bi$_x$/AlSb QW grown on a GaSb substrate (see Supplemental Material [32], Sec. I) within a superlattice electronic structure calculation implemented within a 14 bulk band basis [36] and obtain the zone-center [Γ point, Fig. 1(a)] quantum well states. From those, we derive

momentum matrix elements and the other parameters of the BHZ Hamiltonian. We obtain a crossing between the lowest conduction subbands $|E_1\pm\rangle$ and the highest valence subbands $|HH_1\pm\rangle$ at the critical well thickness $d_c = 6.9$ nm. This crossing characterizes a topological phase transition between an ordinary insulator ($d < d_c$) and a 2D TI ($d > d_c$) with an inverted gap ~ 30 meV [Fig. 1(a)].

Model Hamiltonian for a cylindrical BHZ dot.—We consider the BHZ Hamiltonian describing the low-energy physics of the $|E_1\pm\rangle$ and $|HH_1\pm\rangle$ subbands,

$$\mathcal{H}(\mathbf{k}) = \begin{pmatrix} H(\mathbf{k}) & 0 \\ 0 & H^*(-\mathbf{k}) \end{pmatrix}, \qquad (1)$$

where $H(\mathbf{k}) = (C - D\mathbf{k}^2)\mathbf{1}_{2\times 2} + \mathbf{d} \cdot \boldsymbol{\sigma}$ and $\mathbf{d}(\mathbf{k}) = (Ak_x, -Ak_y, M - B\mathbf{k}^2)$. Here, $\mathbf{k}$ is the in plane wave vector and $\boldsymbol{\sigma}$ are the Pauli matrices describing the pseudospin space. The parameters A, B, C, D and M, calculated within a superlattice $\mathbf{k} \cdot \mathbf{p}$ electronic structure calculation [36], depend on the QW thickness d and are given in Table (S1) of the Supplemental Material [32] for $d = 6$ nm ($x = 0.15$) and $d = 8$ nm ($x = 0.15$). We define our QDs by adding to Eq. (1) the in plane cylindrical confinement [14–26]

$$V_c = \begin{pmatrix} V(r)\sigma_z & 0 \\ 0 & V(r)\sigma_z \end{pmatrix}, \qquad V(r) = \begin{cases} 0 & r < R \\ M_O - M & r > R, \end{cases} \qquad (2)$$

where $M_O - M > 0$ defines the equal strength soft-wall barriers for electrons and holes [37]. Here we focus on the hard-wall case ($M_O \to \infty$), as it is simpler analytically. In the Supplemental Material [32], we discuss the soft-wall case, which qualitatively shows the same behavior.

BHZ dots: Eigensolutions.—We solve $[\mathcal{H}(\mathbf{k}) + V_c]\psi = \varepsilon\psi$ in polar coordinates: $k_x \pm ik_y = -ie^{\pm i\theta}[\partial_r \pm (1/r)\partial_\theta]$ and $k^2 = -[\partial_r^2 + (1/r)\partial_r + (1/r^2)\partial_\theta^2]$. By imposing $\psi(r,\theta) = 0$ at $r = R$, we obtain the transcendental equation for the discrete eigenenergies and eigenfunctions

$$\frac{\lambda_-^2(E_{j_z,n}^\pm) - \frac{E_{j_z,n}^\pm - C - M}{D+B}}{\lambda_-(E_{j_z,n}^\pm)} \frac{I_{j_z\mp\frac{1}{2}}[\lambda_+(E_{j_z,n}^\pm)R]}{I_{j_z\mp\frac{1}{2}}[\lambda_-(E_{j_z,n}^\pm)R]} = \frac{\lambda_+^2(E_{j_z,n}^\pm) - \frac{E_{j_z,n}^\pm - C - M}{D+B}}{\lambda_+(E_{j_z,n}^\pm)} \frac{I_{j_z\mp\frac{1}{2}}[\lambda_+(E_{j_z,n}^\pm)R]}{I_{j_z\mp\frac{1}{2}}[\lambda_-(E_{j_z,n}^\pm)R]}, \qquad (3)$$

$$\psi_{j_z,n}^\pm(r,\theta) = \frac{Ne^{ij_z\theta}}{\sqrt{2\pi}} \begin{bmatrix} \left(I_{j_z\mp\frac{1}{2}}[\lambda_+(E_{j_z,n}^\pm)r] - \frac{I_{j_z\mp\frac{1}{2}}[\lambda_+(E_{j_z,n}^\pm)R]}{I_{j_z\mp\frac{1}{2}}[\lambda_-(E_{j_z,n}^\pm)R]} I_{j_z\mp\frac{1}{2}}[\lambda_-(E_{j_z,n}^\pm)r]\right)e^{\mp i(\theta/2)} \\ \frac{(D+B)\lambda_+^2(E_{j_z,n}^\pm) - E_{j_z,n}^\pm + C + M}{\pm iA\lambda_+(E_{j_z,n}^\pm)} \left(I_{j_z\mp\frac{3}{2}}[\lambda_+(E_{j_z,n}^\pm)r] - \frac{I_{j_z\mp\frac{3}{2}}[\lambda_+(E_{j_z,n}^\pm)R]}{I_{j_z\mp\frac{3}{2}}[\lambda_-(E_{j_z,n}^\pm)R]} I_{j_z\mp\frac{3}{2}}[\lambda_-(E_{j_z,n}^\pm)r]\right)e^{\mp i(3\theta/2)} \end{bmatrix}. \qquad (4)$$

Here $I_{j_z}[\lambda_{\pm}(E^{\sigma}_{j_z,n})r]$. is the modified Bessel function of the first kind, N is a normalization factor, and $\lambda^2_{\pm}(E^{\sigma}_{j_z,n}) = -F \pm \sqrt{F^2 - Q^2}$ with $F = \frac{1}{2}\{[A^2/(D^2 - B^2)] - [(E^{\sigma}_{j_z,n} - C - M)/(D + B)] - [(E^{\sigma}_{j_z,n} - C + M)/(D - B)]\}$ and $Q^2 = [(E^{\sigma}_{j_z,n} - C)^2 - M^2]/(D^2 - B^2)$. The $\pm$ signs in Eqs. (3) and (4) label the "spin" subspaces in the BHZ model (i.e., its two 2×2 blocks) [57] and arise as the time reversal symmetry operator $\Theta = -i\sigma_y \otimes \mathbf{1}_{2 \times 2} K$ commutes with $\mathcal{H}(\mathbf{k})$ in Eq. (1). The $\psi^{\pm}$ states in (4) form a Kramers pair, i.e., $\Theta\psi^+_{j_z,n}(r, \theta) = \psi^-_{-j_z,n}(r, \theta)$. The quantum number j_z corresponds to the z component of the total angular momentum $\mathcal{J}_z = -i\hbar\partial_\theta + \hbar\sigma_z \otimes (\tau_0 - \tau_z/2)$ that obeys $\mathcal{J}_z\psi^{\pm}_{j_z,n}(r, \theta) = \hbar j_z\psi^{\pm}_{j_z,n}(r, \theta)$, $j_z = \pm\frac{1}{2}, \pm\frac{3}{2}, \ldots$. Incidentally, j_z also denotes the parity of the QD states defined via the inversion symmetry operator $\mathcal{I} (r, \theta) \rightarrow (r, \theta + \pi)$, satisfying $\mathcal{I}\psi^{\pm}_{j_z,n}(r, \theta) = (-1)^{j_z \mp \frac{3}{2}}\psi^{\pm}_{j_z,n}(r, \theta)$. Both $\mathcal{J}_z$ and $\mathcal{I}$ commute with the QD Hamiltonian. The quantum number n arises from the radial confinement of the dot; we index our energy spectrum such that, for each j_z and $\sigma(= \pm)$, $n = 1, 2, 3, \ldots$ $(n = -1, -2, -3, \ldots)$ for positive (negative) energies.

In Figs. 1(c)–1(e), we plot the $\text{InAs}_{1-x}\text{Bi}_x$ dot energy levels [Eq. (3)] for *topological* ($x = 0.15$, $d = 8$ nm, $R = 60$ nm), *ordinary* ($x = 0$, $d = 6$ nm, $R = 30$ nm), and *trivial* ($x = 0.15$, $d = 6$ nm, $R = 30$ nm) cases, respectively. The ordinary InAs QD with its noninverted large gap is considered here for comparison (see Supplemental Material [32], Sec. IV). Figures 1(f)–1(h) show the edge and bulk states grouped by the ellipses in Figs. 1(c)–1(e). To gain insight into the origin of the edge states in both topological and nontopological dots, next we look at Eq. (4) in the asymptotic limit $\lambda_\tau(E^{\sigma}_{j_z,n})r \gg m \Rightarrow I_{j_z}[\lambda_\tau(E^{\sigma}_{j_z,n})r] \rightarrow \exp[\lambda_\tau(E^{\sigma}_{j_z,n})r]$ to leading order (this is the parameter range of our Bi-based dots, see Supplemental Material [32], Sec. VI).

For topological BHZ dots ($M < 0$) with $M < E^{\sigma}_{j_z,n} < -M$, we find real $\lambda_{\pm} > 0 \Rightarrow \psi^{\sigma}_{j_z} \approx \hat{a}e^{\lambda_- r} + \hat{b}e^{\lambda_+ r}$ [Eq. (4)], $\hat{a}$, $\hat{b}$ complex spinors (see Supplemental Material [32], Sec. VI). This asymptotic form of $\psi^{\sigma}_{j_z}$ demonstrates its edge state character [Fig. 1(f)] as $\psi^{\sigma}_{j_z}$ peaks near $r = R$ [$\psi^{\sigma}_{j_z}(R) = 0$ for hard wall], similar to that of the 2D TIs. For $E^{\sigma}_{j_z,n} < M$ or $E^{\sigma}_{j_z,n} > -M$, edge and extended ("bulk") states coexist.

Geometrically protected trivial edge states.—For nontopological BHZ dots with $E^{\sigma}_{j_z,n}$ within the valence states [Fig. 1(e)], λ_- is purely imaginary, $\lambda_+ > 0$, and

$$\psi^{\pm}_{j_z}(r) \approx \begin{bmatrix} cJ_{j_z\mp\frac{1}{2}}(|\lambda_-|r) \\ dJ_{j_z\mp\frac{3}{2}}(|\lambda_-|r) \end{bmatrix} + \begin{bmatrix} c_+ \\ d_+ \end{bmatrix} e^{\lambda_+ r}, \quad (5)$$
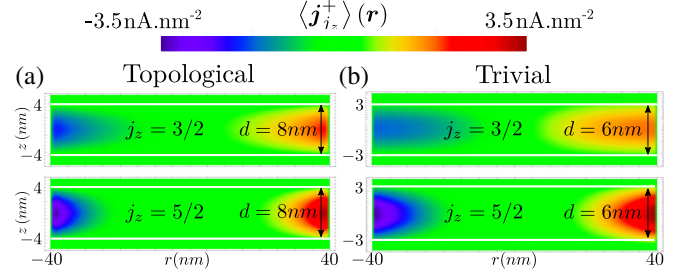
FIG. 2. Spin-up circulating currents for topological (a) and trivial (b) edge states $j_z = \frac{3}{2}$ and $j_z = \frac{5}{2}$ within the gray area in Figs. 1(c) and 1(e). The topological and trivial circulating currents are essentially the same. The horizontal white lines delimit the QW barriers.

where c_+ and d_+ are complex amplitudes. The $J_m(|\lambda_-|r)$'s oscillate with r and have zeros at α^n_m [$J_m(\alpha^n_m) = 0$, $n = 0, 1, 2, 3, \ldots$]. Here, however, they grow monotonically with r within the dot for $E^{\sigma}_{j_z,n}$ in the gray area of Fig. 1(e). This is due to $|\lambda_-|R < \alpha^1_m/2$ for the parameters of our Bi-based BHZ dot in the nontopological regime (see Supplemental Material [32], Sec. VI). Similar to the topological dot case (previous paragraph), $\psi^{\sigma}_{j_z}$ in Eq. (5) peaks near $r = R$ and thus describes "edgelike" states [Fig. 1(h)]. The parameter λ_- controls the degree of localization of the trivial edge states (see Supplemental Material [32], Sec. VI). In addition, as the energies of extended and edgelike states depend differently on the dot radius R, we find that QD confinement precludes the coexistence of some of these states in our nontopological BHZ dots [Fig. 1(e), see also Supplemental Material [32], Sec. VII.] That is, confinement gives rise to a single geometrically protected Kramers pair of dot states per energy within the gray area of Fig. 1(e). This holds for a wide range of QD radii and BHZ parameters (e.g., those of HgTe/CdTe QDs; see also Supplemental Material, Secs. V–VIII [32]).

In contrast, ordinary cylindrical InAs QDs defined from InAs wells with parabolic subbands do not have protected edgelike states [Figs. 1(d) and 1(g)]. These non-BHZ dots have the degeneracies $E^{E_1\pm}_{j_z\mp\frac{1}{2},n} = E^{E_1\pm}_{-j_z\pm\frac{1}{2},n}$ and $E^{HH_1\pm}_{j_z\mp\frac{3}{2},n} = E^{HH_1\pm}_{-j_z\pm\frac{3}{2},n}$, which allow for elastic scattering between these levels, thus precluding protection [58]. This picture still holds in the presence of spin-orbit and electron–heavy-hole mixing effects (see Supplemental Material [32], Sec. IV).

Circulating current densities: $\mathbf{j}(\mathbf{r})$.—We define $\mathbf{j}(\mathbf{r}) = (e\hbar/m_0)\text{Im}\{\psi^{\dagger}(\mathbf{r})\nabla\psi(\mathbf{r})\}$, where the total QD wave function $\psi(\mathbf{r}) = \sum_i F_i(\mathbf{r})u_i(\mathbf{r})$ is expressed as the sum of the product of the periodic part of the Bloch function $u_i(\mathbf{r})$ of band i at the Γ point and its respective envelope function $F_i(\mathbf{r})$. The average current over the unit cell is given by [28,29] $\langle\mathbf{j}\rangle(\mathbf{r}) = (e\hbar/m_0)\text{Im}\sum_{i,j}\{F^*_i(\mathbf{r})F_j(\mathbf{r})\langle u_i|\nabla|u_j\rangle + \delta_{ij}F^*_i(\mathbf{r})\nabla F_j(\mathbf{r})\}$. Using the wave function (4) (see Supplemental Material [32], Sec. IX), we find

$$\langle \boldsymbol{j}^{\pm}_{j_z,n} \rangle (\mathbf{r}) = \pm e \frac{N^2}{2\pi} \left\{ \frac{\sqrt{2}P}{\hbar} |f^{\pm}_1(z)||f^{\pm}_3(z)|I^{j_z \mp \frac{1}{2}}_{E_1,n}(r) I^{j_z \mp \frac{3}{2}}_{HH_1,n}(r) \right.$$

$$\pm \frac{\hbar}{rm_0} \left(j_z \mp \frac{1}{2} \right) [|f^{\pm}_1(z)|^2 + |f^{\pm}_4(z)|^2] |I^{j_z \mp \frac{1}{2}}_{E_1,n}(r)|^2$$

$$\left. \pm \frac{\hbar}{rm_0} \left(j_z \mp \frac{3}{2} \right) |f^{\pm}_3(z)|^2 |I^{j_z \mp \frac{3}{2}}_{HH_1,n}(r)|^2 \right\} \hat{\theta}, \quad (6)$$

where m_0 is the bare electron mass and P is the Kane parameter [29,38,46] appearing due to the coupling between conduction and valence bands. Here, the first term is the "Bloch velocity" contribution to the average current as it stems from the periodic part of the Bloch function, while the second term is the contribution from the envelope function [28,29]. Using $j_z \sim 1$, $P = 0.9055$ eV nm [29], and $r \sim R = 40$ nm, we estimate the ratio of the Bloch to envelope contributions $(\sqrt{2}P/\hbar)/(2 \times \hbar/Rm_0) \sim 340$, thus showing we can neglect the envelope velocity part in agreement with Ref. [29] (see Supplemental Material [32], Sec. IX for a detailed comparison). Since $I^{j_z \mp \frac{1}{2}}_{E_1,n} = I^{-j_z \pm \frac{1}{2}}_{E_1,n}$ and $I^{j_z \mp \frac{3}{2}}_{HH_1,n} = I^{-j_z \pm \frac{3}{2}}_{HH_1,n}$, we find

$$\langle \boldsymbol{j}^{\pm}_{j_z,n} \rangle (\mathbf{r}) = -\langle \boldsymbol{j}^{\mp}_{-j_z,n} \rangle (\mathbf{r}), \quad (7)$$

which shows the helical nature of the edgelike states within the gray region in Figs. 1(c) and 1(e).

To compare the topological QD edge states and the edgelike states in the trivial QD, we plot Eq. (6) in Fig. 2 for the spin-up QD levels $j_z = 3/2$ and $j_z = 5/2$ [see Figs. 1(c) and 1(e), gray area] with $R = 40$ nm. Interestingly, although the $j_z = 3/2$ wave functions of both trivial and topological QDs are extended, their circulating currents are localized near the QD edges. This arises from the product of the upper and lower wave function components in Eq. (6). We find the highest current densities for the trivial edgelike states (due to the smaller d) [Figs. 2(a) and 2(b)]. However, the integrated current density over half of the cross section of the QD $I^{\pm}_{j_z,n} = \int d\boldsymbol{S} \cdot \langle \boldsymbol{j}^{\pm}_{j_z,n} \rangle = \int_0^R dr \int_{-d/2}^{d/2} dz |\langle \boldsymbol{j}^{\pm}_{j_z,n} \rangle| \sim 0.17$ μA for both topological and trivial edge states to within 2%; i.e., it shows no significant difference.

Linear conductance.—To further compare the topological and trivial edgelike states, we calculate the two-terminal linear-response QD conductance $\mathcal{G}$ (at $T = 0$ K) [30] by coupling the dots to left (L) and right (R) leads [Fig. 1(b)]. Our Hamiltonian reads

$$\mathcal{H} = \sum_i \varepsilon_i d^{\dagger}_i d_i + \sum_{k_\alpha,\alpha,\sigma} \varepsilon_{k_\alpha \sigma} c^{\dagger}_{k_\alpha \sigma} c_{k_\alpha \sigma} + \sum_{i,k_\alpha,\alpha,\sigma} V^i_{k_\alpha \sigma} d^{\dagger}_i c_{k_\alpha \sigma}$$

$$+ \sum_{i \neq j} t_{ij} d^{\dagger}_j d_i + \text{H.c.}, \quad (8)$$
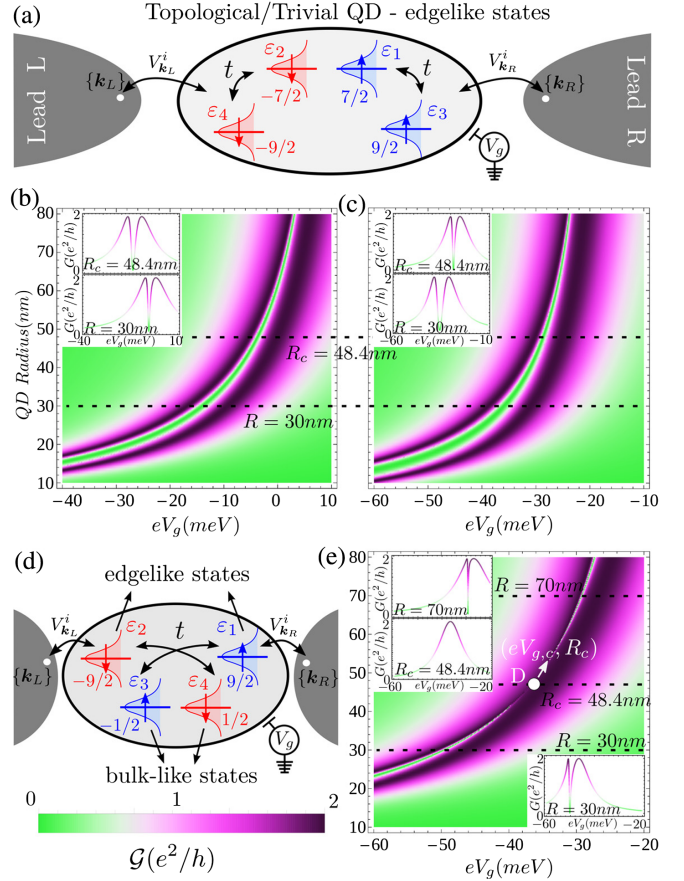
FIG. 3. (a) Schematic QD Hamiltonian for the four topological and trivial edge states with $j_z = \pm 7/2$ and $j_z = \pm 9/2$. QD conductance $\mathcal{G}$ at $T = 0$ K for the topological (b) and trivial (c) edge states in Fig. 3(a). (d) Same as (a) for the coexisting $j_z = \pm 1/2$ bulk and $j_z = \pm 9/2$ edge states and the corresponding $\mathcal{G}$ for the trivial case (e). Here we use $t = 1$ meV and $\Gamma = 4$ meV (see Supplemental Material [32], Sec. X).

where $d^{\dagger}_i$ creates an electron in the QD state $|i\rangle$ [Eq. (4)] with energy $\varepsilon_i = \varepsilon_i(R, V_g)$ [obtained from Eq. (3)], i denotes the set of QD quantum numbers j_z, $\pm$ (or $\uparrow, \downarrow$ [57]), and n (V_g is an additional gate controlling the dot levels with respect to the Fermi energy ε_F of the leads), and $c^{\dagger}_{k_\alpha \sigma}$ creates an electron in the lead $\alpha = L$, R with wave vector k_α, energy $\varepsilon_{k_\alpha \sigma}$, and spin component $\sigma = \uparrow, \downarrow$. The spin-conserving matrix element $V^i_{k_\alpha \sigma}$ denotes the dot-lead coupling, while t_{ij} couples the dot levels. Next we focus on only four QD states with well-defined σ, as shown in Fig. 3(a). This can be achieved by tuning the conduction window and the QD levels via external gates.

Figures 3(b) and 3(c) show the QD conductance $\mathcal{G} = \mathcal{G}_\uparrow + \mathcal{G}_\downarrow$ for the four topological and trivial edge states with $j_z = \pm 7/2$ and $j_z = \pm 9/2$ [see green triangles in Figs. 1(c) and 1(e)], as a function of the QD radius R and the gate potential V_g. The radius R can be varied experimentally through an electrostatic confining potential [59].

The conductance for both the topological and trivial edgelike states show similar behaviors, i.e., double Lorentzian-like profiles centered approximately at the QD levels $\varepsilon_i(R, V_g)$, separated by a dip, and peaked at $2e^2/h$; this is clearly seen in the insets of Figs. 3(b) and 3(c) for two distinct R's. The dip follows from a destructive interference between the two same-spin edge states in the overlapping tails of the broadened QD density of states. See Supplemental Material [32] (Sec. X) where the conductance $\mathcal{G}$ is expressed as a sum of interfering amplitudes using Green functions [47].

Interestingly, bulk- and edgelike valence edge states can coexist and even be degenerate in energy. In this case, our calculated conductances exhibit a crossover from a double-peak resonance for $R < R_c$ nm and $V_g < V_{g,c}$ to a single-peak resonance at $R = R_c$ nm and $V_g = V_{g,c}$ and back to a double-peak resonance for $R > R_c$ nm and $V_g > V_{g,c}$. This is shown in Fig. 3(e) (and its insets) for a trivial QD, but similar behavior also occurs for a topological QD. In the Supplemental Material [32] (Sec. X), we show that, when the bulk- and edge-state Kramers pairs obey $\varepsilon_{3(4)}(R, V_g) - \varepsilon_{1(2)}(R, V_g) = t(V^{3(4)}/V^{1(2)} - V^{1(2)}/V^{3(4)})$, two of the transport channels are completely decoupled from the leads and hence a single resonance (peaked $\mathcal{G} = 2e^2/h$) emerges. For the parameters in Fig. 3(e), this decoupling occurs when the two Kramers pairs (bulk and edge) become degenerate, i.e., $\varepsilon_{1(2)}(R_c, V_{g,c}) = \varepsilon_{3(4)}(R_c, V_{g,c})$ (incidentally, their protection is lost in this case).

Concluding remarks.—We have predicted that Bi-based InAs QWs can become room temperature TIs ($\sim$30 meV) for well widths $d > 6.9$ nm. Our realistic $\mathbf{k} \cdot \mathbf{p}$ approach allows us to calculate the parameters of an effective BHZ model from which we can define cylindrical QDs via further confinement. By solving the BHZ QD eigenvalue equation analytically, we find, quite surprisingly, that both topological and nontopological BHZ QDs feature similar (i) protected helical edge states, (ii) circulating currents, and (iii) two-terminal linear conductances $\mathcal{G}$, exhibiting a two-peak resonance as a function of the QD radius and the gate V_g, controlling its energy levels relative to the Fermi level of the leads. Hence, our proposed cylindrical QDs—topological and nontopological—are equivalent from the standpoint of edge-state transport, in contrast with TIs. We expect that our work will stimulate experimental research on this topic.

[1] C. L. Kane and E. J. Mele, Phys. Rev. Lett. **95**, 226801 (2005).

[2] B. A. Bernevig, T. L. Hughes, and S.-C. Zhang, Science **314**, 1757 (2006).

[3] M. König, S. Wiedmann, C. Brune, A. Roth, H. Buhmann, L. W. Molenkamp, X.-L. Qi, and S.-C. Zhang, Science **318**, 766 (2007).

[4] M. Z. Hasan and C. L. Kane, Rev. Mod. Phys. **82**, 3045 (2010).

[5] C. Liu, T. L. Hughes, X.-L. Qi, K. Wang, and S.-C. Zhang, Phys. Rev. Lett. **100**, 236601 (2008).

[6] Y. Xia *et al.*, Nat. Phys. **5**, 398 (2009).

[7] H. Zhang, C.-X. Liu, X.-L. Qi, X. Dai, Z. Fang, and S.-C. Zhang, Nat. Phys. **5**, 438 (2009).

[8] W. Feng, W. Zhu, H. H. Weitering, G. M. Stocks, Y. Yao, and D. Xiao, Phys. Rev. B **85**, 195114 (2012).

[9] O. P Sushkov and A. H. C. Neto, Phys. Rev. Lett. **110**, 186601 (2013).

[10] D. Zhang, W. Lou, M. Miao, S. C. Zhang, and K. Chang, Phys. Rev. Lett. **111**, 156402 (2013).

[11] S. I. Erlingsson and J. C. Egues, Phys. Rev. B **91**, 035312 (2015).

[12] I. Knez, R.-R. Du, and G. Sullivan, Phys. Rev. Lett. **107**, 136603 (2011).

[13] F. Nichele *et al.*, New J. Phys. **18**, 083005 (2016).

[14] K. Chang and W.-K. Lou, Phys. Rev. Lett. **106**, 206802 (2011).

[15] M. Korkusinski and P. Hawrylak, Sci. Rep. **4**, 4903 (2014).

[16] G. J. Ferreira and D. Loss, Phys. Rev. Lett. **111**, 106802 (2013).

[17] H. P. Paudel and M. N. Leuenberger, Phys. Rev. B **88**, 085316 (2013).

[18] C. Ertler, M. Raith, and J. Fabian, Phys. Rev. B **89**, 075432 (2014).

[19] A. Kundu, A. Zazunov, A. L. Yeyati, T. Martin, and R. Egger, Phys. Rev. B **83**, 125429 (2011).

[20] J. Li, W. K. Lou, D. Zhang, X. J. Li, W. Yang, and K. Chang, Phys. Rev. B **90**, 115303 (2014).

[21] J.-X. Qu, S.-H. Zhang, D.-Y. Liu, P. Wang, and W. Yang, J. Appl. Phys. **122**, 034307 (2017).

[22] H. Xu and Y. C. Lai, Phys. Rev. B **92**, 195120 (2015).

[23] A. A. Sukhanov, Physica (Amsterdam) **513B**, 1 (2017).

[24] S.-N. Zhang, H. Jiang, and H. W. Liu, Mod. Phys. Lett. B **27**, 1350104 (2013).

[25] T. M. Herath, P. Hewageegana, and V. Apalkov, J. Phys. Condens. Matter **26**, 115302 (2014).

[26] B. Scharf and I. Zutić, Phys. Rev. B **91**, 144505 (2015).

[27] B. M. de Resende, F. C. de Lima, R. H. Miwa, E. Vernek, and G. J. Ferreira, Phys. Rev. B **96**, 161113(R) (2017).

[28] J. van Bree, A. Yu. Silov, P. M. Koenraad, and M. E. Flatté, Phys. Rev. B **90**, 165306 (2014).

[29] J. van Bree, A. Yu. Silov, P. M. Koenraad, and M. E. Flatté, Phys. Rev. Lett. **112**, 187201 (2014).

[30] Y. Meir and N. S. Wingreen, Phys. Rev. Lett. **68**, 2512 (1992).

[31] L.-Z. Yao, C. P. Crisostomo, C.-C. Yeh, S.-M. Lai, Z.-Q. Huang, C.-H. Hsu, F.-C. Chuang, H. Lin, A. Bansil, Sci. Rep. **5**, 15463 (2015).

[32] See Supplemental Material at http://link.aps.org/supplemental/10.1103/PhysRevLett.121.256804 for detailed descriptions, which includes Refs. [2,28–30,33–52].

[33] K. Y. Ma, Z. M. Fang, D. H. Jaw, R. M. Cohen, G. B. Stringfellow, W. P. Kosar, and D. W. Brown, Appl. Phys. Lett. **55,** 2420 (1989).

[34] Z. Fang, K. Y. Ma, R. M. Cohen, and G. B. Stringfellow, J. Appl. Phys. **68,** 1187 (1990).

[35] P. T. Webster N. A. Riordan, C. Gogineni, S. Liu, J. Lu, X.-H. Zhao, D. J. Smith, Y.-H. Zhang, and S. R. Johnson, J. Vac. Sci. Technol. B **32,** 02C120 (2014).

[36] W. H. Lau, J. T. Olesberg, and M. E. Flatté, arXiv:cond-mat/0406201.

[37] P. Michetti, P. H. Penteado, J. C. Egues, and P. Recher, Semicond. Sci. Technol. **27,** 124007 (2012).

[38] R. S. Calsaverini, E. Bernardes, J. C. Egues, and D. Loss, Phys. Rev. B **78,** 155313 (2008).

[39] R. Winkler, *Spin-Orbit Coupling Effects in Two-Dimensional Electron and Hole Systems*, Springer Tracts in Modern Physics Vol. 191 (Springer, New York, 2003).

[40] J. Shabani *et al.*, Phys. Rev. B **93,** 155402 (2016).

[41] J. Fu and J. C. Egues, Phys. Rev. B **91,** 075408 (2015).

[42] J. Fu, P. H. Penteado, M. O. Hachiya, D. Loss, and J. C. Egues, Phys. Rev. Lett. **117,** 226401 (2016).

[43] X.-L. Qi and S. C. Zhang, Rev. Mod. Phys. **83,** 1057 (2011).

[44] P. Kasperkovitz, J. Math. Phys. (N.Y.) **21,** 6 (1980).

[45] D. G. Rothe, R. W. Reinthaler, C.-X. Liu, L. W. Molenkamp, S.-C. Zhang, and E. M. Hankiewicz, New J. Phys. **12,** 065012 (2010).

[46] E. O. Kane, J. Phys. Chem. Solids **1,** 249 (1957).

[47] M. L. L. de Guevara, F. Claro, and P. A. Orellana, Phys. Rev. B **67,** 195335 (2003); G.-H. Ding, C. K. Kim, and K. Nahm, Phys. Rev. B **71,** 205313 (2005); H. Lu, R. Lu, and B. F. Zhu, Phys. Rev. B **71,** 235320 (2005).

[48] A.-P. Jauho, N. S. Wingreen, and Y. Meir, Phys. Rev. B **50,** 5528 (1994).

[49] G. Bastard, *Wave Mechanics Applied to Semiconductor Heterostructures* (John Wiley and Sons, New York, 1990).

[50] R. Hanson L. P. Kouwenhoven, J. R. Petta, S. Tarucha, and L. M. K. Vandersypen, Rev. Mod. Phys. **79,** 1217 (2007).

[51] S. Datta, *Electronic Transport in Mesoscopic Systems* (Cambridge University Press, Cambridge, England, 1997).

[52] L. P. Kouwenhoven *et al.*, *Mesoscopic Electron Transport* (Springer, Dordrecht, 1997).

[53] W. Shan, W. Walukiewicz, J. W. Ager, E. E. Haller, J. F. Geisz, D. J. Friedman, J. M. Olson, and S. R. Kurtz, Phys. Rev. Lett. **82,** 1221 (1999).

[54] W. Walukiewicz, W. Shan, K. M. Yu, J. W. Ager, E. E. Haller, I. Miotkowski, M. J. Seong, H. Alawadhi, and A. K. Ramdas, Phys. Rev. Lett. **85,** 1552 (2000).

[55] J. Wu, W. Walukiewicz, and E. E. Haller, Phys. Rev. B **65,** 233210 (2002).

[56] K. Alberi, J. Wu, W. Walukiewicz, K. M. Yu, O. D. Dubon, S. P. Watkins, C. X. Wang, X. Liu, Y.-J. Cho, and J. Furdyna, Phys. Rev. B **75,** 045203 (2007).

[57] Because of the mixing between spin-up ↑ and spin-down ↓ components within the $|E_1\pm\rangle$ subbands, the spin index ↑(↓) is not a good quantum number within the BHZ subspace $+(-)$. However, we calculate $\langle j_z \pm |s_z|j_z\pm\rangle \simeq \pm\hbar/2$; hence it is an excellent approximation to identify the ± subspace with ↑, ↓.

[58] J. I. Climente, C. Segarra, and J. Planelles, New J. Phys. **15,** 093009 (2013).

[59] L. C. Camenzind, L. Yu, P. Stano, J. D. Zimmerman, A. C. Gossard, D. Loss, and D. M. Zumbühl, Nat. Commun. **9,** 3454 (2018).